JOURNAL OF COMPUTATIONAL PHYSICS 72, 243–269 (1987)

Gyrokinetic Particle Simulation Model

W. W. LEE

Plasma Physics Laboratory, Princeton University, Princeton, New Jersey 08544

Received June 27, 1986; revised December 19, 1986

A new type of particle simulation model based on the gyrophase-averaged Vlasov and Poisson equations is presented. The reduced system, in which particle gyrations are removed from the equations of motion while the finite Larmor radius effects are still preserved, is most suitable for studying low frequency microinstabilities in magnetized plasmas. The resulting gyrokinetic plasma is intrinsically quasineutral for $\lambda_D \ll \rho_s$ $(\equiv \rho_i (T_e/T_i)^{1/2})$. Thus, without the troublesome space charge waves in the simulation, we can afford to use much larger time steps $(\omega_H \Delta t \gtrsim 1)$ and grid spacings $(\Delta x_\perp/\rho_s \gtrsim 1)$ at a much reduced noise level than we would have for conventional particle codes, where $\omega_H \equiv (k_\| / k_\perp)(\lambda_D/\rho_s)\,\omega_{pe}$, and $k_\| \ll k_\perp$. Furthermore, it is feasible to simulate an elongated system $(L_\| \gg L_\perp)$ with a three-dimensional grid using the present model without resorting to the usual mode expansion technique, since there is essentially no restriction on the size of $\Delta x_\|$ in a gyrokinetic plasma. The new approach also enables us to further separate the time and spatial scales of the simulation from those associated with global transport through the use of multiple spatial scale expansion. Thus, the model can be a very efficient tool for studying anomalous transport problems related to steady-state drift-wave turbulence in magnetic confinement devices. It can also be applied to other areas of plasma physics. © 1987 Academic Press, Inc

I. INTRODUCTION

Gyrokinetic particle simulation consists of using the existing simulation techniques to solve the gyrophase-averaged Vlasov–Poisson system, in which the particle gyration is removed from the equations of motion while the finite Larmor radius effects are retained [1, 2]. The reduced system has been obtained through the use of well-known gyrokinetic ordering for magnetized plasmas. The resulting nonlinear gyrokinetic equations satisfy the basic requirements for simulation that they preserve the characteristic form of the dynamic equation and satisfy both particle and energy conservation. The new scheme is most useful for studying low frequency gradient-driven microinstabilities in tokamaks. In the previous paper [1], we have demonstrated the feasibility of such an approach. Here, we will present the numerical aspects of the gyrokinetic particle simulation model.

It is generally agreed that conventional particle codes are not practical for studying low frequency quasi-neutral-type of phenomena, because of the disparate time and spatial scales involved. The fundamental problem is the high frequency space charge waves, characterized by ω_{pe} and λ_D, which impose severe restrictions on the time step and spatial resolution used in the code [3, 4]. Even for the model based

0021-9991/87 $3.00

Copyright © 1987 by Academic Press, Inc
All rights of reproduction in any form reserved

on the guiding-center electrons and gyrating (Vlasov) ions [5], which was developed for the purpose of investigating low frequency drift-type instabilities in magnetized plasmas, space charge waves in the form of lower hybrid oscillations still exist. In addition, their presence gives rise to a very high noise level in the simulation plasma, which can actually suppress the growth of the low frequency quasineutral waves, whose equilibrium fluctuation energy is a factor of $(k\lambda_D)^2$ lower. Furthermore, when the saturation amplitude of the instability is lower than the noise level, the nonlinear physics can also be obliterated. To overcome the difficulty of excessive noise by increasing the number of particles in the simulation can be prohibitive. Thus, an unrealistically large background density gradient has to be employed for simulating drift waves in order to produce strong enough instabilities. However, when the scale lengths for the zeroth-order-density and for the perturbation become comparable in magnitude as in Refs. [6–8], profile modification may dominate over other nonlinear processes. Since, under realistic experimental conditions in tokamaks, the background inhomogeneities tend to persist as quasistatic profiles because of the continuous replenishment of plasma particles, it precludes profile relaxation as a viable nonlinear mechanism. Thus, it is difficult to make meaningful comparisons between the simulation results and the experimental observations. These are some of the pitfalls confronting the conventional particle codes in simulating low frequency waves.

In our present model, the difficulties associated with space charge waves no longer exist, since a gyrokinetic plasma is intrinsically quasineutral for $\lambda_D \ll \rho_s$ $(\equiv \rho_i (T_e/T_i)^{1/2})$, where ρ_i is the ion gyroradius. Following the procedures developed by Langdon [3, 4] based on the leap-frog scheme for particle pushing and linear interpolation for charge sharing, we have found that the limitations on the time step and the grid spacing become much less stringent for the gyrokinetic model. Instead of the usual $\omega_{pe}\,\Delta t \gtrsim 1$ and $\Delta x \gtrsim \lambda_D$ for unmagnetized plasmas, the stability conditions now become $\omega_H\,\Delta t \gtrsim 1$ and $\Delta x_\perp \gtrsim \rho_s$, where $\omega_H \equiv (k_\parallel/k_\perp)(m_i/m_e)^{1/2}\,\Omega_i \equiv (k_\parallel/k_\perp)(\lambda_D/\rho_s)\,\omega_{pe}$ is the electrostatic shear-Alfven wave frequency, $\Omega_i \equiv eB/m_i c$, $k_\parallel \ll k_\perp \cong k$, and subscripts $\parallel$ and $\perp$ denote quantities parallel and perpendicular to the external magnetic field, respectively. Results from the numerical analysis of our model also indicate that there is essentially no limitation on the size of $\Delta x_\parallel$. Compared with the guiding-center electron code [5], where the time step is limited by $\omega_{pi}\,\Delta t \gtrsim 1$ and grid spacing by $\Delta x_\perp = \Delta x_\parallel \gtrsim \lambda_D$, the present scheme represents orders of magnitude improvement.

For reasons of accuracy rather than stability, the Courant condition of $k_\parallel v_{te}\,\Delta t \equiv (\omega_H\,\Delta t)(k_\perp \rho_s) \gtrsim 1$ imposed by the electron transit time also has to be satisfied in our simulation. For $k_\perp \rho_s \cong 1$ modes, which usually have the largest growth rates for microinstabilities and are the most important ones in the simulation, this condition does not constitute an additional constraint. The restriction of $k_\perp v_E\,\Delta t \gtrsim 1$, where $\mathbf{v}_E \equiv c\mathbf{E} \times \mathbf{B}/B^2$, is usually not a problem for tokamak plasmas. In the presence of a sheared magnetic field, as we will discuss, normal modes associated with ω_H do not exist at all and local instabilities due to $\omega_H \Delta t > 1$ are also absent. Therefore, the time step in the simulation can be solely determined by the mode frequency of interest (e.g., the diamagnetic drift frequency, ω_*). The scheme for satisfying the additional requirement of $(k_{\|})_{\max} v_{te} \Delta t \gtrsim 1$ will be discussed.

The restriction on $\Delta x_\perp$ poses no difficulty at all for the gyrokinetic model. A grid of the size of ρ_s is needed, at any rate, to resolve accurately the fluctuations for the modes with $k_\perp \rho_s \cong 1$, which, as we have mentioned before, are the most important ones in the simulation.

As for the three-dimensional simulation, we can now afford to use a very coarse grid in the parallel direction for which $\Delta x_{\|} \gg \rho_s$ to model an elongated system with $L_{\|} \gg L_\perp$. Thus, the mode expansion technique [9] commonly used in the conventional codes is not the only alternative here. The grid instability, which may still exist in the 3D gyrokinetic simulation when modes with $k_\perp \rho_s \ll 0.21$ are included, can be suppressed by the higher order interpolation schemes [10]. The combination of finite-size particle effets and implicit particle pushing schemes [11] can also stabilize all the numerical instabilities caused by $\omega_H \Delta t > 1$, usually related to $k_\perp \rho_s \ll 1$ modes in the 3D code. However, most interestingly, all the alias-induced numerical growths mentioned here may altogether be eliminated by magnetic shear, on which we will elaborate.

Because of the nature of the gyrophase-averaging processes [1, 2], the gyrokinetic Vlasov equation is expressed in the gyrocenter coordinates, whereas the original particle coordinates are retained for the gyrokinetic Poisson equation. To circumvent the numerical difficulties involving coordinate transformations, the simulation scheme described in Ref. [1] used the analytically transformed gyrokinetic Vlasov equation in the particle variable space by assuming that, nonlinearly, ion perpendicular temperature is zero. In the present paper, we have developed an efficient numerical method to expedite the transformation, which can accurately represent the gyrophase-averaged quantities for arbitrary values of $k_\perp \rho_i$, linearly as well as nonlinearly. As for the gyrokinetic Poisson equation, it is a linear second-order differential equation in our regime of interest and can be solved by an iterative scheme.

The fact that the reduced Vlasov equation is in the gyrocenter coordinates makes it possible for us to perform the multiple scale expansion on the spatial derivative term of the equation so as to separate the equilibrium spatial scale lengths from those of the perturbations. In doing so, the zeroth-order density and temperature gradients become input parameters for the simulation. By holding them constant in time, we succeed in removing from the simulation the time and spatial scales associated with global transport. Since the model now contains only the frequency and the spatial scale of interest, it is most suitable for studying steady-state drift-wave turbulence problems. Furthermore, the application of multiple spatial scale expansion also simplifies the boundary conditions for the particles and waves in the simulation, which, in turn, greatly facilitates the diagnotics for particle nd energy transport.

Finally, one important aspect of the gyrokinetic plasma is its low noise level. This important property has been investigated in Ref. [12], in which the equilibrium fluctuation field energy is shown to be at a minimum in the gyrokinetic regime. Thus, for the same number of particles, we can simulate a much larger volume of plasma with the present model than with conventional codes.

In recent years, various implicit schemes have been developed for the purpose of eliminating unwanted high frequency oscillations from the simulation through numerical means [11, 13–15]. These approaches represent a basic difference in philosophy from the scheme considered in this paper, where the removal of the space charge waves is contingent upon the underlying physics. Other numerical methods to achieve long time step simulation have also been developed based on orbit averaging [16] and electron subcycling [17]. Under certain conditions, some of these numerical schemes can be very useful for us.

The paper is organized as follows. In Section II, the governing equations in an electrostatic slab and their conservation properties are described. The pertinent numerical schemes are presented in Section III. Section IV discusses the simulation schemes based on multiple spatial scale expansion. Numerical properties of the gyrokinetic plasma are presented in Section V. Some relevant simulation results are described in Section VI, and discussion and concluding remarks are given in Section VII.

II. GYROKINETIC FORMALISM

The gyrophase-averaged Vlasov and Poisson equations have been derived earlier [1, 2] based on the well-known gyrokinetic ordering, which assumes that ω/Ω, ρ/L, $k_{\|}/k_{\perp}$, and $e\Phi/T$ are of order ε, where ω is the frequency of interest, Ω is the gyrofrequency, ρ is the gyroradius, L is the equilibrium scale length, $k_{\|}$ and $k_{\perp}$ are the perturbed wave numbers parallel and perpendicular to the magnetic field, respectively, $e\Phi/T$ is the electrostatic potential normalized to average plasma temperature, and ε is a smallness parameter. The gyrophase-averaging procedure not only removes the gyrophase-dependent quantities from the reduced system, but also eliminates the fast gyromotion which gives rise to the unwanted high frequency waves, while retaining the important finite Larmor radius effects.

The resulting gyrokinetic Vlasov equation in slab geometry valid to order ε^2 can be written in terms of gyrocenter variables as [1, 2]

$$\begin{aligned} DF/Dt \equiv \partial F/\partial t + v_{\|}\hat{\mathbf{b}} \cdot \partial F/\partial \mathbf{R} - (q/m\Omega)(\partial \Psi/\partial \mathbf{R} \times \hat{\mathbf{b}}) \cdot \partial F/\partial \mathbf{R} \\ - (q/m)(\partial \Psi/\partial \mathbf{R} \cdot \hat{\mathbf{b}})\, \partial F/\partial v_{\|} = 0. \end{aligned} \tag{1}$$

where

$$\Psi(\mathbf{R}) \equiv \bar{\Phi}(\mathbf{R}) - (q/2T)(v_t/\Omega)^2\, |\partial \Phi(\mathbf{R})/\partial \mathbf{R}_{\perp}|^2, \tag{2}$$

$F \equiv F(\mathbf{R}, \mu, v_{\|}, t)$ is the gyrophase-independent distribution function, $\mu \equiv v_{\perp}^2/2$, $\Omega \equiv qB/mc$, $\hat{\mathbf{b}} \equiv \mathbf{B}/B$, $\mathbf{B}$ is the external magnetic field, $v_t \equiv (T/m)^{1/2}$, $\Phi(\mathbf{R})$ and $\bar{\Phi}(\mathbf{R})$

are the electrostatic potentials at the gyrocenter, and q is the signed charge. Moreover, the gyrocenter position variable $\mathbf{R}$ is related to the particle position variable $\mathbf{x}$ through $\mathbf{R} \equiv \mathbf{x} - \boldsymbol{\rho}$, where $\boldsymbol{\rho} \equiv -\mathbf{v}_\perp \times \hat{\mathbf{b}}/\Omega$ is the particle gyroradius. Equation (1) is valid for both the electrons and the ions. However, for the electrons, the finite gyroradius effects are negligible and Eq. (1) reduces to the usual drift-kinetic equation for $\boldsymbol{\rho} \rightarrow 0$.

The gyrokinetic Poisson equation in particle coordinates takes the form of [1, 2]

$$\nabla^2 \Phi - \tau(\Phi - \tilde{\Phi})/\lambda_D^2 + (\rho_s/\lambda_D)^2 \nabla_\perp \cdot \{(n_i - n_0) \nabla_\perp \Phi/n_0\} = -4\pi e(\bar{n}_i - n_e), \quad (3)$$

where the electrostatic potentials Φ and $\tilde{\Phi}$ as well as the number density $\bar{n}_i$, n_i, and n_e are functions of $\mathbf{x}$, $\nabla \equiv \partial/\partial \mathbf{x}$, $\lambda_D^2 \equiv T_e/4\pi n_0 e^2$, $\tau \equiv T_e/T_i$, $\rho_s \equiv \sqrt{\tau} \rho_i$, $\rho_i \equiv (T_i/m_i)^{1/2}/\Omega_i$, and subscripts e and i denote species. The distribution function, potential, and number density in Eqs. (1), (2), and (3) can be related through the Fourier transforms of

$$\Phi(\mathbf{x}) = \sum_{\mathbf{k}} \Phi(\mathbf{k}) \exp(i\mathbf{k} \cdot \mathbf{x}) \qquad \text{and} \qquad F(\mathbf{R}) = \sum_{\mathbf{k}} F(\mathbf{k}) \exp(i\mathbf{k} \cdot \mathbf{R}).$$

The coordinate-transformed quantities then become

$$\bar{\Phi}(\mathbf{R}) = \sum_{\mathbf{k}} \Phi(\mathbf{k}) J_0(k_\perp v_\perp/\Omega) \exp(i\mathbf{k} \cdot \mathbf{R}), \quad (4)$$

$$\bar{n}(\mathbf{x}) = \sum_{\mathbf{k}} \int F(\mathbf{k}) J_0(k_\perp v_\perp/\Omega) \exp(i\mathbf{k} \cdot \mathbf{x}) \, d\mu \, dv_\parallel, \quad (5)$$

and

$$\tilde{\Phi}(\mathbf{x}) = \sum_{\mathbf{k}} \Phi(\mathbf{k}) \Gamma_0(b) \exp(i\mathbf{k} \cdot \mathbf{x}), \quad (6)$$

where the ordinary Bessel function

$$J_0 = \langle \exp(i\mathbf{k} \cdot \boldsymbol{\rho}) \rangle_\varphi \quad (7)$$

is the result of the gyrophase-averaging process, $\Gamma_0(b) \equiv I_0(b) \exp(-b)$ comes from the second gyrophase averaging with respect to the Maxwellian background, $b = k_\perp^2 \rho_i^2$, I_0 is the modified Bessel function, $\Phi(\mathbf{R})$ and $n(\mathbf{x})$ correspond, respectively, to $\bar{\Phi}(\mathbf{R})$ and $\bar{n}(\mathbf{x})$ with $J_0 = 1$, and $n_0 \equiv \langle n(\mathbf{x}) \rangle_{\mathbf{x}}$ is the spatially averaged number density. In Eq. (3), $\rho_e = 0$ is assumed, and the additional terms on the left-hand side of the equation are the contributions from the ion polarization density response. For $b \ll 1$, the lowest order term becomes $(\rho_s/\lambda_D)^2 \nabla_\perp^2 \Phi$. Since $\rho_s \gg \lambda_D$ for the usual tokamak plasmas, the Debeye shielding term of $\nabla^2 \Phi$ is much smaller by comparison and, thereby, can be ignored in Eq. (3). (This is true for arbitrary value of b.) Finally, in Eqs. (2) and (3), we have kept only the leading terms from the small gyroradius expansion for $O(\varepsilon^2)$ quantities, i.e., terms of $O(k_\perp^4 \rho_i^4 \Phi^2)$ are ignored. This approximation considerably simplifies the numerical scheme and can be justified on physics grounds.

The Hamiltonian nature of our equations [2] allows us to obtain simple expressions for various conservation laws for Eqs. (1)–(3). From the simulation point of view, the most relevant ones are particle and energy conservation. The former is rather trivial and can be verified by taking the zeroth moment of Eq. (1) in $(\mathbf{R}, \mu, v_{\|})$ space. The energy conservation, which can be derived by following the procedure given in Ref. [2] takes the form of

$$\begin{aligned}\sum_{\alpha=e,i} m_\alpha \left\langle \int (\mu + v_{\|}^2/2)\, F_\alpha \, d\mu \, dv_{\|} \right\rangle_{\mathbf{R}} &+ (1/8\pi) \sum_{\mathbf{k}} k^2\, |\Phi(\mathbf{k})|^2 \\ &+ (\tau/8\pi\lambda_D^2) \sum_{\mathbf{k}} [1-\Gamma_0(b)]\, |\Phi(\mathbf{k})|^2 \\ &+ (\rho_s^2/8\pi n_0 \lambda_D^2) \langle |\partial\Phi(\mathbf{x})/\partial\mathbf{x}_\perp|^2\, [n_i(\mathbf{x}) - n_0] \rangle_{\mathbf{x}} = \text{const},\end{aligned} \tag{8}$$

where $\langle \cdots \rangle$ denotes spatial average in the appropriate coordinate system. The first two terms can be readily identified as the usual particle kinetic energy and electrostatic potential energy, respectively. The last two are the ion sloshing energy; the second one comes from the $O(\varepsilon^2)$ terms in Eqs. (2) and (3). For $b \ll 1$, we have

$$\text{sloshing energy/potential energy} \cong (\omega_{pi}/\Omega_i)^2 \equiv (\rho_s/\lambda_D)^2.$$

Thus, for $\rho_s \gg \lambda_D$, most of the field energy in the gyrokinetic plasma is associated with the ion sloshing motion in the perpendicular direction in response to the electrostatic fluctuations. Consequently, the potential energy, which is related to the $\nabla^2\Phi$ term in Eq. (3), is negligible.

III. NUMERICAL TECHNIQUES

In this section, we will discuss the numerical schemes for solving the gyrokinetic Vlasov–Poisson system, Eqs. (1)–(3), based on, for the most part, the existing explicit particle simulation techniques. Applying the discrete representation for the distribution function of N particles,

$$F = \sum_{j=1}^{N} \delta(\mathbf{R} - \mathbf{R}_j)\, \delta(\mu - \mu_j)\, \delta(v - v_{\|j}), \tag{9}$$

to Eq. (1), we obtain the equations of motion in the gyrocenter coordinates for the jth gyrokinetic particle as

$$d\mathbf{R}_j/dt = v_{\|j}\hat{\mathbf{b}} - (q/m\Omega)(\partial\Psi/\partial\mathbf{R} \times \hat{\mathbf{b}})\,|_{\mathbf{R}_j,\mu_j} \tag{10}$$

and

$$dv_{\|j}/dt = -(q/m)\, \partial\Psi/\partial\mathbf{R} \cdot \hat{\mathbf{b}}\,|_{\mathbf{R}_j,\mu_j}, \tag{11}$$

where Ψ is the gyrophase-averaged potential defined in Eqs. (2) and (4). Equations (10) and (11) reduce to the familiar guiding-center equations of motion for the drift-kinetic particles when $\rho = 0$ (or $\mu = 0$). Thus, the only difference between the two types of particles is in the form of the electrostatic potential with which they interact. Consequently, the leap-frog and/or the predictor-corrector schemes for pushing the drift-kinetic particles described in Ref. [5] can also be used here for the particles, once Ψ is known. However, the method for calculating Ψ for each individual particle is complicated by the appearance of J_0 in the equation for $\bar{\Phi}$.

The gyrokinetic Poisson equation, Eq. (3), in the Fourier $\mathbf{k}$ space becomes

$$\begin{aligned}(k\lambda_D^2)\,\delta\Phi(\mathbf{k})+\tau[1-\Gamma_0(b)]\,\delta\Phi(\mathbf{k})+\sum_{\mathbf{k}=\mathbf{k}_1+\mathbf{k}_2}(\mathbf{k}_{1\perp}\cdot\mathbf{k}_{2\perp}+k_{2\perp}^2)\,\rho_s^2\,\delta n_i(\mathbf{k}_1)\,\delta\Phi(\mathbf{k}_2)&\\ =[\delta\bar{n}_i(\mathbf{k})-\delta n_e(\mathbf{k})],&\qquad(12)\end{aligned}$$

where $\delta\Phi \equiv e\Phi/T_e$, $\delta n \equiv (n-n_0)/n_0$, $\delta\bar{n} \equiv (\bar{n}-n_0)/n_0$, with $\bar{n}$, as well as n, defined in Eq. (5). Because of the presence of the $O(\varepsilon^2)$ terms, Eq. (12) is in the form of an inhomogeneous Fredholm equation of the second kind and can easily be solved using the method of successive approximation [18], once the particle number densities are given. Here, again, the difficulty comes from the evaluation of $\bar{n}$, which involves J_0.

As we can see, Eqs. (10)–(12) can be solved straightforwardly with the standard numerical methods. The only issue remaining is the coordinate transformations of Eqs. (4) and (5). Since the calculation of J_0 using table lookup for each individual particle to account for its interaction with all the waves in the system is computationally prohibitive, alternative methods are needed. One obvious way is to carry out the transformation analytically at the sacrifice of some important physics as reported in Ref. [1]. A better approach is to use the power series expansion of $J_0 \cong 1-(k_\perp\rho)^2/4+(k_\perp\rho)^4/64\cdots$. The drawbacks here are the additional computer storage (arrays) required for the calculation and the unphysical behavior at large $k_\perp\rho$ when the resulting $|J_0|$ becomes larger than 1.

The scheme we are about to discuss is efficient, more versatile, more physical in nature and needs no additional storage. The starting point for its derivation is to rewrite Eqs. (4) and (5) as

$$\bar{\Phi}(\mathbf{R})=\left\langle\int\Phi(\mathbf{x})\,\delta(\mathbf{x}-\mathbf{R}-\boldsymbol{\rho})\,d\mathbf{x}\right\rangle_\varphi,\qquad(13)$$

and

$$\bar{n}(\mathbf{x})=\left\langle\int F(\mathbf{R},\mu,v_\parallel)\,\delta(\mathbf{R}-\mathbf{x}+\boldsymbol{\rho})\,d\mathbf{R}\,d\mu\,dv_\parallel\right\rangle_\varphi,\qquad(14)$$

where $\langle\ \rangle_\varphi \equiv \oint d\varphi/2\pi$ denotes gyrophase average. Equations (13) and (14) can be easily verified using the relation of Eq. (7). From

$$\Phi(\mathbf{x}_j)=\int\Phi(\mathbf{x})\,\delta(\mathbf{x}-\mathbf{x}_j)\,d\mathbf{x},\qquad(15)$$

where $\mathbf{x}_j = \mathbf{R}_j + \boldsymbol{\rho}_j$ is the actual position of the jth particle, we have

$$\bar{\Phi}(\mathbf{R}_j) = \langle \Phi(\mathbf{x}_j) \rangle_\varphi = \sum_{\mathbf{k}} \Phi(\mathbf{k})\, J_0(k_\perp v_{\perp j}/\Omega) \exp(i\mathbf{k} \cdot \mathbf{R}_j). \tag{16}$$

Thus, the potential at the gyrocenter position $\mathbf{R}_j$ is the gyrophase-averaged potential of the particle at its actual position $\mathbf{x}_j$ as it traverses a circular path centered at $\mathbf{R}_j$ with the gyroradius ρ_j. Analytically, J_0 accounts for the difference between the potential measured directly at $\mathbf{R}_j$ and the average potential.

By substituting Eq. (9) into Eq. (14), the expression for number density in terms of individual particle positions can be obtained as

$$\bar{n}(\mathbf{x}) = \sum_{j=1}^{N} \langle \delta(\mathbf{x} - \mathbf{x}_j) \rangle_\varphi = \sum_{\mathbf{k}} \left(\sum_{j=1}^{N} \exp(-\mathbf{k} \cdot \mathbf{R}_j)\, J_0(k_\perp v_{\perp j}/\Omega)/V \right) \exp(i\mathbf{k} \cdot \mathbf{x}), \tag{17}$$

where V is the total volume. Here, the relation of

$$\delta(\mathbf{x}) = \sum_{\mathbf{k}} \exp(i\mathbf{k} \cdot \mathbf{x})/V$$

is used in the derivation. Again, J_0 accounts for the difference between calculating the number density at $\mathbf{R}_j$ and at $\mathbf{x}_j$. Equation (17) also relates the number density at $\mathbf{x}$ with the gyrophase-averaged contribution from the individual particle as it travels in a circular path. In other words, for calculating $\bar{n}(\mathbf{x})$, each gyrokinetic particle can be viewed as a uniformly charged ring with its center located at $\mathbf{R}_j$ and with radius ρ_j.

Thus, through Eqs. (16) and (17), we have established the correspondence between the gyrophase-averaging procedures in the Fourier $\mathbf{k}$ space and those in the ($\mathbf{x}/\mathbf{R}$) configuration space. The latter is apparently much more suitable for numerical calculations. More specifically, the evaluation of $\bar{\Phi}(\mathbf{R}_j)$ for the jth particle from the known potential field $\Phi(\mathbf{x})$, given by Eq. (12), can be carried out by simply taking the average of $\Phi(\mathbf{x}_j)$'s for a number of locations on a circle, where $\mathbf{x}_j = \mathbf{R}_j + \boldsymbol{\rho}_j$. We can then use this $\bar{\Phi}(\mathbf{R}_j)$ to calculate $\Psi(\mathbf{R}_j)$ in Eq. (2) for the actual potential of the particle. For pushing particles with Eqs. (10) and (11), one can utilize the equivalent operation of

$$\partial\bar{\Phi}(\mathbf{R})/\partial\mathbf{R}\,|_{\mathbf{R}_j,\mu_j} = \langle \partial\Phi(\mathbf{x})/\partial\mathbf{x}\,|_{\mathbf{x}_j} \rangle_\varphi \tag{18}$$

to evaluate the field for each particle, in which the $O(\varepsilon^2)$ part can be calculated directly at $\mathbf{R}_j$. Likewise, the evaluation of $\bar{n}(\mathbf{x})$ can be carried out by summing up the contributions from the gyrokinetic particles represented by rings of charges. For each individual particle at $\mathbf{R}_j$, the charge is equally distributed in a number of locations of $\mathbf{x}_j$'s on a circle. The resulting $\bar{n}(\mathbf{x})$ then becomes the input for Eq. (12).

The issue now is to determine the optimal number of points (locations) on a ring for the accurate representation of the gyrophase-averaging procedure. This is critical because it directly affects the computational time and, ultimately, determines

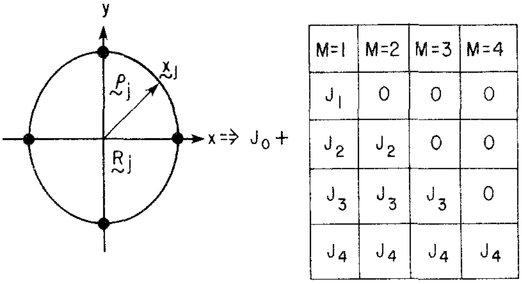

M=1	M=2	M=3	M=4
J_1	0	0	0
J_2	J_2	0	0
J_3	J_3	J_3	0
J_4	J_4	J_4	J_4

FIG 1. Numerical scheme for coordinate transformation for the jth particle.

the viability of the scheme. One way to tackle the problem is to study the result of numerical integration of $\exp(i\mathbf{k}\cdot\boldsymbol{\rho})$ in Eq. (7) for various $\Delta\varphi$'s. Obviously, a large number of integration steps, or a small $\Delta\varphi$, is most accurate, but undesirable. Letting $\Delta\varphi = 2\pi/M$, where M is the number of integration steps, we can easily show that

$$\begin{aligned}\langle\exp(i\mathbf{k}\cdot\boldsymbol{\rho})\rangle_\varphi &= \sum_{n=-\infty}^{\infty} J_n(k_\perp\rho)\sum_{l=1}^{M}\exp(i2\pi nl/M)/M \\ &= \sum_{n=-\infty}^{\infty} J_n(k_\perp\rho)\sin(2\pi n)\cot(n\pi/M)/2M. \qquad (19)\end{aligned}$$

As we can see, for $M=1$, all J_n's have nonvanishing coefficients. Therefore, it is the poorest representation for the gyrophase-averaging process. In the other limit, for $M=\infty$, we recover Eq. (7). The numerical scheme for coordinate transformation and the results for using different values of M in Eq. (19) are shown in Fig. 1. Since $J_0 \gg J_4$ for $k_\perp\rho \lesssim 2$, the scheme with $M=4$ is most ideal for studying microturbulence, where the experimental measurements have indicated that the majority of the fluctuation energy is in the region of $0<k_\perp\rho_i \lesssim 1$ [19]. Thus, a four-point representation for the gyrokinetic particle is adequate for calculating $\bar{\Phi}(\mathbf{R}_j)$ and $\bar{n}(\mathbf{x})$ in Eqs. (16) and (17). For those particles with $k_\perp\rho > 2$ in the simulation, the scheme does not describe their behavior correctly. However, the resulting $\langle\exp(i\mathbf{k}\cdot\boldsymbol{\rho})\rangle_\varphi$ is always much less than one. Thus, the problem is not serious at all compared with the J_0 expansion scheme. If the physics for $k_\perp\rho > 2$ is important, one should then use a larger M for the calculation. For the electrons, where $\rho = 0$, the difference between $\mathbf{R}_j$ and $\mathbf{x}_j$ disappears. Hence, the scheme with $M=1$ is sufficient, which is simply the usual guiding-center model for the drift-kinetic particles [5].

IV. MULTIPLE SPATIAL SCALE EXPANSION

As stated earlier, the purpose of multiple spatial scale expansion is to enable us to develop a numerical model which simulates the realistic experimental condition, where, insofar as microinstabilities are concerned, the background inhomogeneity is quasistatic. Let us start with the expansion of

$$\partial F/\partial \mathbf{R}_\perp \Rightarrow \varepsilon(\partial F/\partial \varepsilon \mathbf{R}_\perp) + \partial F/\partial \mathbf{R}_\perp, \tag{20}$$

where $\varepsilon \mathbf{R}_\perp$ represents the spatial variations for the zeroth-order quantity, and $\mathbf{R}_\perp$ is now associated with the scale lengths of the perturbations only. Assuming that

$$F_0 \equiv (1/\sqrt{2\pi})\, n_0(\varepsilon \mathbf{R}_\perp)[m/T_0(\varepsilon \mathbf{R}_\perp)]^{3/2} \exp[-mv^2/2T_0(\varepsilon \mathbf{R}_\perp)], \tag{21}$$

is the background distribution, we find

$$\varepsilon(\partial F/\partial \varepsilon \mathbf{R}_\perp) \cong -\mathbf{K}F, \tag{22}$$

where

$$\mathbf{K} \cong [\boldsymbol{\kappa}_n - (3/2 - v^2/2v_t^2)\, \boldsymbol{\kappa}_T], \tag{23}$$

$\boldsymbol{\kappa}_n \equiv -\varepsilon(\partial n_0/\partial \varepsilon \mathbf{R}_\perp)/n_0$, $\boldsymbol{\kappa}_T \equiv -\varepsilon(\partial T_0/\partial \varepsilon \mathbf{R}_\perp)/T_0$, and $v^2 \equiv v_\parallel^2 + v_\perp^2$. Substituting Eqs. (20) and (22) into Eq. (1), we then obtain

$$DF/Dt + (q/m\Omega)(\partial \Psi/\partial \mathbf{R} \times \hat{\mathbf{b}}) \cdot \mathbf{K}F = 0, \tag{24}$$

in which the scale lengths for the background and the perturbations are completely separated, and the distribution F contains only spatial variations for the perturbations. Equation (24) is similar to the equation used in many theoretical analyses. The only difference comes from the term associated with the background inhomogeneity $\mathbf{K}$, for which the distribution function F, for example, is replaced by F_0 in Eq. (21) [20–22], or by a spatially averaged F.

However, Eq. (24) is not suitable for particle pushing because it lacks the conservation properties. The proper equation can be constructed from Eq. (24). It takes the form of

$$DF/Dt + (q/m\Omega)[(\partial F/\partial \mathbf{R} \times \hat{\mathbf{b}}) \cdot \mathbf{K}\Psi + (\partial \Psi/\partial \mathbf{R} \times \hat{\mathbf{b}}) \cdot \mathbf{K}F] = 0. \tag{25}$$

Equation (25) conserves number of particles and, together with Eq. (3), also conserves energy. The latter is again given by Eq. (8). Since the multiple spatial scale expansion is based on $|\mathbf{k}| \gg |\mathbf{K}|$, the difference between the nonlinear physics described by Eqs. (24) and (25) is rather insignificant and is of higher order in ε, provided that modes with $|\mathbf{k} \cdot \mathbf{K}/K| < |K|$ for Ψ are excluded from Eq. (25).

Equations of motion for the individual particles given by Eq. (25) can be derived using the distribution function F defined in Eq. (9). They become

$$d\mathbf{R}_j/dt = v_{\parallel j}\hat{\mathbf{b}} - (q/m\Omega)(\partial \Psi/\partial \mathbf{R} \times \hat{\mathbf{b}} + \mathbf{K} \times \hat{\mathbf{b}}\Psi)\,|_{\mathbf{R}_j, \mu_j}, \tag{26}$$

and

$$dv_{\parallel j}/dt = -(q/m)\, \partial \Psi/\partial \mathbf{R} \cdot \hat{\mathbf{b}}\,|_{\mathbf{R}_j, \mu_j}, \tag{27}$$

for the jth particle. The important feature here is that Eqs. (26) and (27) differ from the original gyrokinetic equations of motion, Eqs. (10) and (11), by only one term; and it is the term which accounts for the effect of background inhomogeneity. Thus, by keeping $\boldsymbol{\kappa}_n$ and $\boldsymbol{\kappa}_T$ constant in time (and space), we can indeed investigate steady-state microturbulence problems with the new set of equations. As for the initial loading in the simulation, one can use spatially uniform distribution for the particles (with the Maxwellian distribution in the velocity space, if desired) at $t = 0$, since the distribution function F in Eqs. (24) and (25) describes only spatial perturbations. Thus, not surprisingly, the separation of the disparate spatial scales in the simulation makes it possible for us to study gradient-driven microinstabilities using homogeneous plasmas. Moreover, the freezing of the background inhomogeneity also effectively removes the global transport time scale from the simulation. Thus, Eqs. (26) and (27), as well as Eq. (25), contain only the spatial and time scales of interest, in which the undesirable scales have been eliminated analytically beforehand (through the processes of gyrophase averaging and multiple spatial scale expansion). The idea of multiple spatial scale expansion was first proposed by the authors of Ref. [23].

It should be mentioned here that the particle dynamics depicted by Eq. (25) are no longer incompressible in the $(\mathbf{R}, \mu, v_{\|})$ phase space. Nevertheless, the fact that particle simulation techniques are still applicable in this case can be understood as follows. Rewriting Eq. (9) as

$$F(\mathbf{Z}) = \sum_{j=1}^{N} \delta(\mathbf{Z} - \mathbf{Z}_j), \tag{28}$$

where $\mathbf{Z} \equiv (\mathbf{R}, \mu, v_{\|})$ or the original phase space variables $(\mathbf{x}, \mathbf{v})$, one can show that particle pushing is actually solving an equation of the type

$$\partial F/\partial t + (\partial/\partial \mathbf{Z}) \cdot (\dot{\mathbf{Z}} F) = 0, \tag{29}$$

where $\dot{\mathbf{Z}}$ $(\equiv d\mathbf{Z}/dt)$ is the equation of motion. This is exactly the form for Eq. (25). When the phase space fluid is incompressible, i.e. $(\partial/\partial \mathbf{Z}) \cdot \dot{\mathbf{Z}} = 0$. Eq. (29) reduces to Eq. (1) (or the Vlasov equation). Thus, incompressibility is not the prerequisite for particle pushing.

Let us now discuss the diagnostics for the particle and energy flux for the new scheme. As stated earlier, these measurements are greatly facilitated by the use of multiple spatial scale expansion and are quite different from those in which the background inhomogeneities are actually present. Applying Eq. (20) to Eq. (1) and taking the zeroth moment in $(\mu, v_{\|})$ of the resulting equation as well as by performing the spatial average, we have

$$\partial n_0/\partial t + (\partial/\partial \varepsilon \mathbf{x}) \cdot [n_0 \langle \boldsymbol{\Gamma} \rangle_{\mathbf{x}}] = 0, \tag{30}$$

where

$$\boldsymbol{\Gamma} = -(c/B)[(\partial \Phi/\partial \mathbf{x} \times \hat{\mathbf{b}})(\bar{n}/n_0) - (1/2)(q/T)(v_t/\Omega)^2 \, (\partial/\partial \mathbf{x}) \, |\partial \Phi/\partial \mathbf{x}_{\perp}|^2 \times \hat{\mathbf{b}}(n/n_0)] \tag{31}$$

is the particle flux, and n_0, $\bar{n}$, and n are defined in Eq. (3). For $\boldsymbol{\kappa}_n = \kappa_n \hat{\mathbf{x}}$, i.e., the density gradient is in the x direction, the particle diffusion coefficient becomes

$$D = \langle \Gamma_x \rangle_{\mathbf{x}} / \kappa_n. \tag{32}$$

Particle flux $\boldsymbol{\Gamma}$ can also be expressed in terms of individual particle motion. With the substitution of Eq. (17) into Eq. (31), the flux in the x direction can be written as

$$\langle \Gamma_x \rangle_{\mathbf{x}} = \sum_{j=1}^{N} v_{Ex}(\mathbf{R}_j)/N, \tag{33}$$

where $v_{Ex} \equiv -(c/B)(\partial \Psi / \partial \mathbf{R}) \times \hat{\mathbf{b}} \cdot \hat{\mathbf{x}}$ is the particle drift, and the evaluation of which involves the use of Eq. (18). The calculation of Eq. (33) for the electrons is considerably simplified, since $\rho = 0$ and $\mathbf{R}_j = \mathbf{x}_j$. Multiplying Eq. (3) by $-(c/B)(\partial \Phi / \partial \mathbf{x}) \times \hat{\mathbf{b}} \cdot \hat{\mathbf{x}}$ and invoking the periodic boundary conditions for the potentials, we arrive at

$$\langle \Gamma_{ex} \rangle_{\mathbf{x}} = \langle \Gamma_{ix} \rangle_{\mathbf{x}}, \tag{34}$$

where the flux is given by Eq. (31). Thus, particle flux is ambipolar for our system.

Before we examine the issue of energy flux, let us describe briefly the gyrokinetic expressions for some of the related fluid quantities in the simulation. Following the same procedures in obtaining Eqs. (14) and (17) for the number density, we find that the current density can be evaluated by

$$\bar{J}_{\|}(\mathbf{x}) = q \left\langle \int v_{\|} F(\mathbf{R}, \mu, v_{\|}) \, \delta(\mathbf{R} - \mathbf{x} + \boldsymbol{\rho}) \, d\mathbf{R} \, d\mu \, dv_{\|} \right\rangle_{\varphi} = q \sum_{j=1}^{N} v_{\| j} \langle \delta(\mathbf{x} - \mathbf{x}_j) \rangle_{\varphi}, \tag{35}$$

and the expression for the energy density is

$$\begin{aligned} \bar{P}(\mathbf{x}) &= (m/3) \left\langle \int v^2 F(\mathbf{R}, \mu, v_{\|}) \, \delta(\mathbf{R} - \mathbf{x} + \boldsymbol{\rho}) \, d\mathbf{R} \, d\mu \, dv_{\|} \right\rangle_{\varphi} \\ &= (m/3) \sum_{j=1}^{N} v_j^2 \langle \delta(\mathbf{x} - \mathbf{x}_j) \rangle_{\varphi}. \end{aligned} \tag{36}$$

Thus, the numerical calculations of these quantities are similar to the manner in which number density is obtained as depicted in Fig. 1.

The method for measuring energy flux in the simulation can now be derived as follows. Applying Eq. (20) to Eq. (1) and taking the v^2 moment of the resulting equation, we obtain, after performing the spatial average,

$$\partial P_0 / \partial t + (\partial / \partial \varepsilon \mathbf{x}) \cdot [P_0 \langle \mathbf{Q} \rangle_{\mathbf{x}}] = \langle S \rangle_{\mathbf{x}}, \tag{37}$$

where $P_0 \equiv \langle \bar{P}(\mathbf{x}) \rangle_{\mathbf{x}}$ is the average energy density,

$$\mathbf{Q} = -(c/B)[(\partial\Phi/\partial\mathbf{x} \times \hat{\mathbf{b}})(\bar{P}/P_0) - (1/2)(q/T)(v_t/\Omega)^2 \, (\partial/\partial\mathbf{x}) \, |\partial\Phi/\partial\mathbf{x}_\perp|^2 \times \hat{\mathbf{b}}(P/P_0)] \tag{38}$$

is the energy flux,

$$S = -(2/3)[\bar{J}_{||}(\partial\Phi/\partial x_{||}) - (1/2)(q/T)(v_t/\Omega)^2 \, \bar{J}_{||}(\partial/\partial x_{||}) \, |\partial\Phi/\partial\mathbf{x}_\perp|^2] \tag{39}$$

is the source term, with $\bar{J}$ and $\bar{P}$ given by Eqs. (35) and (36), and P corresponds to $\bar{P}$ with $\rho = 0$. For $J_{||0} \equiv \langle \bar{J}_{||}(\mathbf{x}) \rangle_{\mathbf{x}} = 0$, which gives $P_0 = n_0 T_0$, and for $\boldsymbol{\kappa}_n = \kappa_n \hat{\mathbf{x}}$, and $\boldsymbol{\kappa}_T = \kappa_T \hat{\mathbf{x}}$. Eq. (37) yields the thermal diffusivity in the inhomogeneous x direction as

$$\chi = \langle Q_x \rangle_{\mathbf{x}} / (\kappa_n + \kappa_T). \tag{40}$$

Energy flux can also be measured through individual particle motion. Substituting Eq. (36) into Eq. (38), we obtain

$$\langle Q_x \rangle_{\mathbf{x}} = \sum_{j=1}^{N} v_{Ex}(\mathbf{R}_j)(v_j/v_t)^2/3N, \tag{41}$$

where v_{Ex} is again the particle drift defined in Eq. (33). Likewise, with the substitution of Eq. (35) into Eq. (39), the spatially averaged source term becomes

$$\langle S \rangle_{\mathbf{x}} = \sum_{j=1}^{N} v_{||j}(\partial\Psi/\partial\mathbf{R} \cdot \hat{\mathbf{b}})|_{\mathbf{R}_j}, \tag{42}$$

in which the use of Eq. (18) is again necessary for the calculation.

Thus, the ease with which the flux and diffusion measurements can be carried out using the present simulation scheme is evident. It differs greatly from conventional particle simulation, for which the only effective tool is the measurement of test particle diffusion. However, test particle diffusion does not give any information on particle and energy flux. Such information can only be ascertained through the study of the global features of the simulation. The difficulty here is that the simulation volume in the conventional codes is usually too small to be able to describe the global phenomena accurately. This deficiency is removed by the present simulation scheme with the multiple spatial scale expansion. By doing so, we can now view the simulation plasma as a small segment of a much larger system (as if we are dealing with a homogeneous plasma). By allowing the simulation plasma to interact with the neighboring system through the appropriate use of boundary conditions for the waves and the particles, we can study a variety of realistic problems without simulating the total plasma volume. For such an arrangement, the global flux and diffusion of the simulation can be construed as the local quantities for the larger system. One simple example is the use of periodic boundary conditions for the investigation of gradient-driven microinstabilities in a shearless slab [20–22].

V. Numerical Properties

Numerical properties for the simulation plasma using the Vlasov particles have been extensively investigated since the inception of particle simulation more than two decades ago [24, 25]. [illegible] step ($\omega_{pe} \Delta t \gtrsim 1$) [4] and grid spacing ($\Delta x \gtrsim \lambda_D$) [3]. In this section, we will follow the same procedures as in Refs. [3, 4] to establish the stability criteria for the gyrokinetic plasma.

The starting point is the linear dispersion relation for a gyrokinetic plasma in slab geometry obtained from Eqs. (1)–(3).

$$D \equiv 1 + \frac{1}{(k\lambda_D)^2}\left[1 + \tau + \left(1 - \frac{\omega_*}{\omega}\right) X_e + \left(\tau + \frac{\omega_*}{\omega}\right) X_i \Gamma_0\right] = 0, \tag{43}$$

where

$$X_\alpha \equiv \frac{\omega}{\sqrt{2} k_\parallel v_{t\alpha}} Z\left(\frac{\omega}{\sqrt{2} k_\parallel v_{t\alpha}}\right), \tag{44}$$

Z is the usual plasma function, $\omega_* \equiv k_y \rho_s \kappa_n \rho_s \Omega_i$ is the diamagnetic drift frequency produced by the density gradient in the x direction, $\Gamma_0 \cong 1 - (k_\perp \rho_i)^2$ for small $k_\perp \rho_i$, and α denotes species. For the cold plasma response ($\omega / k_\parallel \gg v_{t\alpha}$) and $\omega_* = 0$, the eigenmode frequencies for Eq. (43) are

$$\omega^2 = \omega_H^2 \equiv \left(\frac{k_\parallel}{k_\perp}\right)^2 \left(\frac{m_i}{m_e}\right) \Omega_i^2 \equiv \left(\frac{k_\parallel}{k_\perp}\right)^2 \left(\frac{\lambda_D}{\rho_s}\right)^2 \omega_{pe}^2 \tag{45}$$

for $\rho_s \gg \lambda_D$. These are the damped quasineutral oscillations, which can be identified as electrostatic shear-Alfven waves. (The modification of ω_H by ω_* is small and is negligible for the analysis.) Our focus here is to understand the stability properties of these modes in relation to the sizes of the time and space steps used in the simulation. Their contribution to equilibrium fluctuations will also be examined.

We begin the numerical analysis by first rewriting Eq. (44) as

$$X_\alpha \equiv -1 + (k_\parallel v_{t\alpha})^2 \int_0^\infty t \exp\{i\omega t - (k_\parallel v_{t\alpha} t)^2/2\}\, dt. \tag{46}$$

By letting $t = q\,\Delta t$, the integral here can be evaluated numerically by

$$\int_0^\infty dt \Rightarrow \sum_{q=0}^{\infty} \Delta t. \tag{47}$$

Langdon has elegantly demonstrated that the size of the integration step Δt in Eq. (47) corresponds directly to the time step used in the leap-frog particle pushing scheme in the simulation [4]. Substituting the discrete form for X_α into Eq. (43), and invoking the quasineutral condition and the cold ion approximation, we arrive at

$$D\left(\frac{\lambda_D}{\rho_s}\right)^2 \equiv 1+(\omega_H \Delta t)^2 \sum_{q=0}^{\infty} q \exp\left[i(\omega \Delta t)\, q-\frac{1}{2}(\omega_H \Delta t)^2 (k_\perp \rho_s)^2 q^2\right]=0, \quad (48)$$

for $k \cong k_\perp \gg k_\parallel$. By keeping only the first nontrivial term in the series, we find that the maximum growth of the unphysical instability, if it exists, occurs at $(k_\perp \rho_s)(\omega_H \Delta t)=\sqrt{2}$. The corresponding growth rate is $\omega_I \Delta t = 2 \ln(\omega_H \Delta t) - 1$, which gives the onset of the instability at $\omega_H \Delta t = 1.65$ with $k_\perp \rho_s = 0.86$, and yields larger growths for the smaller $k_\perp \rho_s$'s. Thus, the stability condition can roughly be expressed as

$$\omega_H \Delta t \lesssim 1. \quad (49)$$

As in Ref. [4], the instability originates from the aliasing effects on a temporal grid. The dispersion relation for an unmagnetized plasma and the resulting stability criterion given by Ref. [4] can also be recovered from Eqs. (48) and (49) through the substitutions of ω_H and ρ_s by ω_{pe} and λ_D, respectively. Besides the stability consideration, the time step also has to satisfy the particle transit time requirement of

$$k_\parallel v_{te} \Delta t \equiv (k_\perp \rho_s)(\omega_H \Delta t) \lesssim 1, \quad (50)$$

so that accurate plasma response, i.e., Eq. (48), can be reproduced in the simulation. The difference between Eqs. (49) and (50) is that violation of the latter will not lead to numerical instability. Nonetheless, both equations have to be satisfied in the simulation. Since microinstabilities are generally most unstable for the modes with $k_\perp \rho_s \cong 1$ and their inclusion in the simulation is essential, the two conditions then become identical. Thus, there is no reason to further increase $\omega_H \Delta t$ (except for 3D simulation, which we will discuss). This is quite different from the unmagnetized cases, in which implicit schemes can be utilized to increase $\omega_{pe} \Delta t$ in simulating $k\lambda_D \ll 1$ modes [11, 13, 14]. As we can see, orders of magnitue improvement in time step over the conventional codes is indeed realized with the present scheme without resorting to implicit particle pushing. The condition of $k_\perp v_E \Delta t \lesssim 1$ can usually be satisfied without any difficulty and does not constitute an additional constraint.

In the presence of shear, radial eigenmodes associated with ω_H do not exist at all. This property has been verified using a mode equation of the form, $\partial^2\Phi/\partial x^2 + Q(\omega, \Delta t)\,\Phi = 0$, obtained from Eq. (43) for $\Gamma_0 \cong 1-(k_y \rho_i)^2+\rho_i^2(\partial^2/\partial x^2)$ and $k_\parallel = k_y x/L_s$, where L_s is the shear scale length. Analytically, for $\omega_* = 0$ and $\Delta t \to 0$, its absence can be understood from the fact that modes from the ω_H branch do not satisfy the outgoing wave boundary condition and have no spatially evanescent solutions (away from the rational surface at $k_{\|}=0$). The mode equation has also been solved numerically using a WKB-shooting code [26]. The results have indicated that the only eigenmodes in the system are those associated with ω_*, and instabilities induced locally due to $k_{\|} v_{te} \Delta t > 1$ and $\omega_H \Delta t > 1$ away from the rational surface are also absent. The only requirement needed in this case is that

$$\omega \Delta t < 1 \tag{51}$$

(e.g., $\omega \Delta t = 0.1$ or 0.2), and it is for the purpose of accurately describing the temporal behavior of the wave, where ω is the eigenmode frequency. These important results from the WKB-shooting code have also been confirmed by the gyrokinetic simulation of drift instabilities in a sheared slab [1]. It is, of course, a highly desirable situation, where the time step is solely determined by the mode frequency of interest. However, there is a caveat.

The fact that correct physics can be reproduced in the region where $k_{\|} v_{te} \Delta t > 1$ is rather fortuitous for this case with a single rational surface. Because the amplitude of the mode is very, very small in this region, the error caused by $X_e \cong i\omega \Delta t$ (instead of zero) is inconsequential. In general, one would not want to violate Eq. (50). Thus, even with the elimination of the modes related to ω_H by shear, the electron transit time requirement still has to be taken into account in the simulation. Interestingly, a gyrokinetic plasma under the influence of shear has the unique property of slow waves (low frequency eigenmodes) coexisting with fast particles (thermal electrons), i.e., $\omega / k_{\|} v_{te} \ll 1$, in the region away from the rational surface. Therefore, it is the most natural system for the application of the orbit averaging [16] or electron subcycling [17] schemes, and it requires no implicitness. This important feature also exists in the finite-β gyrokinetic plasma even in the absence of shear [27].

The scheme can work as follows. One pushes the ions and solves the field equation with a time step that satisfies Eq. (51), $\omega \Delta t \lesssim 1$, while calculating the electron orbits with a time step of $(k_{\|})_{\max} v_{te} \Delta t_e \lesssim 1$, where $\Delta t / \Delta t_e = N_t$ with $N_t \gg 1$. For successive Δt_e's, the fields experienced by the electrons are constant in time, since they evolve on a much slower time scale than the electron transit time, i.e., $\omega \ll (k_{\|})_{\max} v_{te}$. Moreover, by accumulating the information on the number density for the electrons for the successive Δt_e's, one needs N_t times less particles for the electrons than for the ions to achieve the same statistical accuracy. Therefore, the number of numerical operations under this subcycling scheme remains the same as that of a system which pushes particles with a time step prescribed by Eq. (51), i.e., the frequency of interest.

The restrictions on grid spacings, $\Delta x_{\perp}$ and $\Delta x_{\|}$, for a gyrokinetic plasma can be studied using the procedures similar to those in Refs. [3, 4]. Here, Gaussian-shaped particles with the widths of $a_{\perp}$ and $a_{\|}$ are assumed. For $k_{\|} a_{\|} \ll 1$, $k_{\|} \Delta x_{\|} \ll 1$, and $k \cong k_{\perp} \gg k_{\|}$, Eq. (48) becomes

$$D\left(\frac{\lambda_D}{\rho_s}\right)^2 \equiv 1+(\omega_H \Delta t)^2 \exp(-k_\perp^2 a_\perp^2)$$
$$\times \sum_{p=-\infty}^{\infty} (k_p/k_\perp)(W(k_p \Delta x_\perp/2))^n$$
$$\times \sum_{q=0}^{\infty} q \exp\left[i(\omega \Delta t)\, q-\frac{1}{2}(\omega_H \Delta t)^2 (k_p\rho_s)^2 q^2\right]=0, \tag{52}$$

where

$$W(\theta)\equiv \sin\theta/\theta$$

is the shape function, $k_p \equiv k_\perp - 2\pi p/\Delta x_\perp$, and n represents different charge sharing schemes [3, 10, 28]. The additional harmonics for $p \neq 0$ are due to the nonphysical aliases arising from the use of a spatial grid. By assuming $k_\perp a_\perp \ll 1$ and $\omega_H \Delta t \ll 1$ and keeping only $p=0$ and ± 1 terms in Eq. (52), we arrive at

$$D\left(\frac{\lambda_D}{\rho_s}\right)^2 \equiv 1-(\omega_H/\omega)^2 (W(k_\perp \Delta x_\perp/2))^n$$
$$+\frac{1}{(k_\perp\rho_s)^2} \sum_{p=-1,1}^{\infty} (k_\perp/k_p)(W(k_p \Delta x_\perp/2))^n$$
$$\times\left(1+i\sqrt{\pi/2}\left(\frac{\omega}{|k_p|\, v_{te}}\right)\exp\left[-\frac{\omega^2}{2(k_p v_{te})^2}\right]\right)=0. \tag{53}$$

It can be shown that the largest numerical growth from Eq. (53), based on the NGP ($n=2$) scheme, occurs at $k_\perp \Delta x_\perp \cong \pi/1.4$ for $k_\perp \rho_s \cong 0.21$, i.e., $\Delta x_\perp/\rho_s \cong 11$. Numerical solutions from Eq. (52) also indicate that, in general, this type of instability becomes insignificant for

$$\Delta x_\perp \lesssim \rho_s, \tag{54}$$

if one uses the linear interpolation ($n=4$) scheme. The usual unmagnetized results can be recovered from Eqs. (52)–(54) by dropping the subscript $\perp$, and substituting ω_H and ρ_s by ω_{pe} and λ_D, respectively. (So, the results here are not really surprising.) Since ρ_s is at least $1 \sim 2$ orders of magnitude larger than λ_D for tokamak plasmas, Eq. (54) indeed represents a significant improvement. Furthermore, Eq. (54) is not really a restriction, because one is compelled to use a grid spacing of $\Delta x_\perp \lesssim \rho_s$ to provide the necessary resolution for modes with $k_\perp \rho_s \cong 1$. Thus, we are again in a best possible situation where the grid size is prescribed by the physical process of interest. This is quite different from the conventional simulation,

[redacted]

in the parallel direction, $\Delta x_{\|}$, can be derived from Eqs. (52) and (53) by making the following substitutions: $k_\perp a_\perp \to k_{\|} a_{\|}$, $k_p \Delta x_\perp \to k_{\|p} \Delta x_{\|}$, where $k_{\|p} \equiv k_{\|} - 2\pi p/\Delta x_{\|}$. The resulting equations are valid for $k_\perp a_\perp \ll 1$ and $k_\perp \Delta x_\perp \ll 1$. Specifically, Eq. (52), after the substitutions, yields

$$\begin{aligned} D\left(\frac{\lambda_D}{\rho_s}\right)^2 &\equiv 1 + (\omega_H \Delta t)^2 \exp(-k_{\|}^2 a_{\|}^2) \\ &\quad \times \sum_{p=-\infty}^{\infty} \left(\frac{k_{\|p}}{k_{\|}}\right)\left(W(k_{\|p} \Delta x_{\|}/2)\right)^n \\ &\quad \times \sum_{q=0}^{\infty} q \exp\left[i(\omega \Delta t)\, q - \frac{1}{2}(\omega_H \Delta t)^2 (k_p \rho_s)^2 (k_{\|p}/k_{\|})^2 q^2\right] = 0. \end{aligned} \tag{55}$$

One important characteristic of the equation is that $k_{\|}$ and $k_\perp$ and, in turn, $\Delta x_{\|}$ and $\Delta x_\perp$ are coupled through ω_H. Following the previous derivation based on the NGP scheme, we can show that the largest growth occurs at $k_{\|} \Delta x_{\|} \cong \pi/1.4$ for $k_\perp \rho_s \cong 0.21$ regardless of the size of $\Delta x_{\|}$—a rather unique feature. Numerical solutions from Eq. (55) indicate that the instability for $k_\perp \rho_s \gtrsim 0.21$ modes can be suppressed by using the linear interpolation scheme ($n = 4$) together with finite size particles. However, for $k_\perp \rho_s \ll 0.21$ modes, total stabilization may have to come from the quadratic interpolation scheme ($n = 6$). Although we have not studied the influence of shear on the behavior of grid instabilities, there are good reasons to believe that some degree of stabilization may occur. This view is supported in part by the recent study on finite-β gyrokinetic plasmas, which has shown that grid instability can be totally suppressed by (a very small amount of) magnetic perturbation [27]. At any rate, since there are essentially no restrictions on $\Delta x_{\|}$, one can use a three-dimensional grid for an elongated system ($L_{\|} \gg L_\perp$) to simulate tokamak-type problems. The mode expansion scheme [9], which circumvents the use of a grid in the elongated direction, is a powerful tool but has its share of drawbacks as well.

A brief discussion on the time step issue for the 3D gyrokinetic simulation is in order here. In general, Δt is determined by the largest ω_H (or the smallest $k_\perp \rho_s$) in the system, which may be much larger than the frequency of interest. Thus, the use of $\omega_H \Delta t \gg 1$ may be desirable and we have to deal with the problem of numerical growth. While instabilities due to large $k_{\|}$'s associated with the smallest $k_\perp \rho_s$ can be suppressed by finite-size particles effects; those caused by small $k_{\|}$'s can only be eliminated by implicit schemes [11, 13, 14]. This is permissible, since the unstable modes all have $k_\perp \rho_s \ll 1$. However, as stated earlier, numerical growths due to large $\omega_H \Delta t$ are no longer a problem in the presence of shear and the electron subcycling scheme is applicable here as well.

Let us now compare the stability conditions of the gyrokinetic plasma with other models of magnetized plasmas. As we all know, the properties for unmagnetized plasmas are similar to those for the model based on full particle dynamics [30] in which λ_D limits the sizes for both $\Delta x_\perp$ and $\Delta x_{\|}$. As for the model using drift-kinetic electrons and Vlasov ions [5], the restrictions become $\omega_{pi} \Delta t \gtrsim 1$ and

$\Delta x_{\parallel} = \Delta x_{\perp} \gtrsim \lambda_D$ (assuming $T_e = T_i$). These conditions can easily be verified with the procedure described here with the assumption of unmagnetized ions. The main advantage of the model is the improvement in time step over the full dynamics code by a factor of $\sqrt{m_i/m_e}$. The drift-kinetic model [31], which is not useful for tokamak physics, exists in the opposite limit of the gyrokinetic model, i.e., $\rho_s \ll \lambda_D$. It has the properties of $(k_{\parallel}/k)\,\omega_{pe}\,\Delta t \gtrsim 1$ and $\Delta x_{\perp} \gtrsim \lambda_D$. The stability condition on $\Delta x_{\parallel}$ in this case is similar to the gyrokinetic model except for the fact that the characteristic length involved is λ_D. All three models discussed here contain space charge waves.

The last topic of this section concerns the issue of numerical noise. Langdon [32] has conducted a detailed analysis on the subject for the Vlasov plasma, which indicates that the fluctuations (and the noise) in the simulation and the usual theoretical predictions are in good agreement for $kv_t\,\Delta t \gtrsim 1$ and $\Delta x \gtrsim \lambda_D$. Thus, if we prescribe Eq. (50) for electron transit time and Eq. (54) for grid spacing, kinetic theory results can also be used to examine the noise issue in our model. Applying Eq. (43) to the fluctuation-dissipation theorem, one finds, for $k\lambda_D \ll 1$,

$$|E(\mathbf{k}, \omega_H)|^2/8\pi \cong (\lambda_D/\rho_s)^2\, T/2, \tag{56}$$

which is a factor of $(\lambda_D/\rho_s)^2$ smaller than the fluctuation energy in a plasma where space charge waves are present. This salient feature has been investigated in Ref. [12] and it is found that the equilibrium electric field energy is at minimum in the gyrokinetic regime. As such, the numerical noise due to the discrete particle effects is also the lowest. In terms of fluctuating potentials, Eq. (56) can also be written as

$$|e\Phi(\mathbf{k}, \omega_H)/T| \cong 1/(\sqrt{N}k\rho_s). \tag{57}$$

where N is the total number of simulation particles (electrons or ions) in a wavelength of $2\pi/k$. Since the thermal noise level in the usual simulation codes is $|e\Phi(\mathbf{k})/T| \cong 1/(\sqrt{N}k\lambda_D)$, the noise in the gyrokinetic plasma is reduced by a factor of λ_D/ρ_s for the same number of simulation particles. (An example of this property is shown in Figs. (1) and (2) in Ref. [1]. For tokamak-type parameters, the gain is much higher.)

As we know, excessive noise tends to suppress the weaker instabilities, which is the reason why large density gradients have been used in the previous simulations of drift instabilities [6–8]. The process involved has not been well understood. Here, we will try to provide an explanation. One may argue that the noise-induced damping that overcomes the linear growth γ_l is caused by enhanced particle diffusion. Dupree's resonance broadening process [33] relates the damping increment to diffusion through $\Delta\gamma = k^2 D$ (for $k \cong k_{\perp}$). To estimate D, let us use the random walk model [34] which yields

$$D = (\Delta x)^2/2\,\Delta t \cong \Delta(e\Phi/T)\,|_{rms}\,\rho_s^2 \Omega_i/2. \tag{58}$$

Assuming that $\Delta(e\Phi/T)\,|_{rms}$ is given by Eq. (57), which is an upper bound estimate, we obtain

$$\Delta\gamma/\Omega_i \cong k\rho_s/2\sqrt{N} \cong (k\rho_s)^2\,|e\Phi/T|/2 \tag{59}$$

for the gyrokinetic plasma. By comparison, the noise-induced damping rate in the Vlasov plasma, $\Delta\gamma/\Omega_i \cong (k\rho_s)^2/(2\sqrt{N}k\lambda_D)$, is much larger for the same N. Thus, we can afford to use milder (more realistic) density and temperature gradients to simulate weaker instabilities with the present scheme.

Nevertheless, the condition of $\Delta\gamma < \gamma_l$ for the modes of interest should always be satisfied in the simulation. This is supported by the simulation results reported in Refs. [1, 7, 20]. The condition, in turn, determines the allowable initial fluctuation amplitude and the total number of particles required for the simulation. For example, in the case of drift waves in slab geometry, where $k_\perp\rho_s \cong 1$ modes are most unstable, Eq. (59) gives $\Delta\gamma/\Omega_i \approx |e\Phi/T|$. Letting $\gamma_l \approx \omega_*$, we obtain a rough estimate for the allowable initial noise level as

$$|e\Phi/T|_{t=0} < \rho_s/L_n, \tag{60}$$

where $L_n(\equiv 1/|\kappa_n|)$ is the density scale length. It is commonly agreed that the saturation amplitude for these type of modes can be approximated by $|e\Phi/T|_{t=\infty} \cong \rho_s/L_n$ [21]. Thus, the condition imposed by Eq. (60) for the initial perturbation also agrees with the fact that the initial amplitude should be lower so that the nonlinear physics after saturation is not obscured by the noise. The derivation here makes the connection between the two requirements. Furthermore, all the modes in the simulation with a fixed $k_\parallel$ associated with γ_l, should also satisfy Eq. (60) initially, because Eq. (57) is constant for all the corresponding **k**'s in this case. The consequence is that the total number of particles in the simulation is given by $N_{\text{total}} = \text{const} \times (L_\perp)^2$, where $L_\perp$ is the size in the perpendicular direction. This is true regardless of the size of the grid. Since the computer resources determine the maximum allowable N_{total} in the simulation, they ultimately restrict the plasma volume for the gyrokinetic particle simulation.

Thus, the only real limitation for our model comes from the noise consideration. Nevertheless, based on the current understanding of microturbulence in tokamaks [35], and with the availability of the present generation of supercomputers, realistic simulation can indeed be carried out with the model, which we will demonstrate later.

VI. SIMULATION RESULTS

At the present time, a two-dimensional $(x, y, \mu, v_\parallel)$ gyrokinetic particle code in slab geometry based on the techniques described in Sections III and IV has been developed. Here, we will use it to verify the numerical properties of the gyrokinetic plasma as predicted in Section V and to demonstrate, by way of an example of drift instability, the utility and the usefulness of the multiple spatial scale expansion scheme (Section IV).

In the simulation, the external magnetic field $\mathbf{B} \equiv B_0(\hat{\mathbf{Z}} + \theta_B \hat{\mathbf{y}})$, is in the $y-z$ plane, where $|\theta_B| \ll 1$ is a constant (shear-free), and the zeroth-order plasma inhomogeneity is in the x direction, i.e., $\mathbf{K} \equiv K\hat{\mathbf{x}}$, where $\mathbf{K}$ is defined in Eq. (23). For [redacted] imposed by the multiple spatial scale expansion, we have also set $\Phi(m=0, n \neq 0)=0$ in the code. Particle pushing is accomplished through the use of the predictor-corrector scheme [5] for finite-size particles [24, 25].

Let us first present the simulation results for a homogeneous plasma. The parameters, in units of grid size $\Delta x_\perp$ and ion cyclotron frequency Ω_i, are: $L_x \times L_y$ (simulation volume) $= (16 \times 16)\,\Delta x_\perp$, N_{total} (simulation particles per species) $=$ 64×64, $m_i/m_e = 1837$, $T_e/T_i = 1$, $a_\perp$ (particle size)$/\Delta x_\perp = 1$, $\theta_B = k_\parallel/k_y = 0.01$, $(k_x\,\Delta x_\perp, k_y\,\Delta x_\perp) \cong (0.4m, 0.4n)$, where $(m, n) = 0$, ± 1, ± 2,..., and $\Omega_i\,\Delta t$ (time

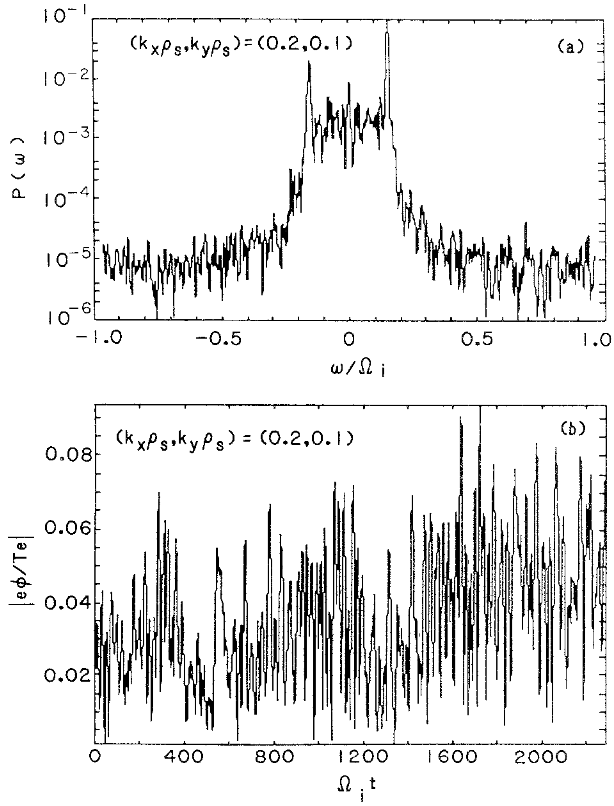

FIG. 2. Frequency spectrum (a) and amplitude evolution (b) of $e\Phi/T_e$ for $\rho_s/\Delta x_\perp = 0.25$ in a homogeneous plasma in thermal equilibrium.

step) = 3.27, which gives $\omega_H \Delta t\,|_{\max} = 1.4$ and $\omega_H(m=n)\,\Delta t = 1$. The total number of time steps is $t_{\max}/\Delta t = 700$.

For $\rho_s/\Delta x_\perp = 0.25$, all the modes in the simulation are stable. The frequency spectrum of the electrostatic potential $e\Phi(2, 1)/T_e$, for which $(k_x\rho_s, k_y\rho_s) \cong (0.2, 0.1)$, and the time evolution of the mode amplitude are shown in Figs. 2a and 2b, respectively. The normal mode frequencies are slightly below the predicted values of $\omega_H/\Omega_i = \pm 0.19$ given by Eq. (45), and the maximum fluctuation amplitude is also somewhat below the theoretical value of 9.8 % obtained from Eq. (57). A more careful numerical calculation using Eq. (52) with $n = 4$ (linear interpolation scheme) gives $\omega/\Omega_i = \pm 0.15 - i0.0045$, which are in excellent agreement with the results in Fig. 2a. The resulting spectrum also reveals that most of the fluctuation energy resides with the normal modes of the system, although there is some enhancement for $|\omega| < |\omega_H|$. The enhancement, which is probably of the nonlinear nature and can become even more pronounced for some of the modes in the simulation, will not cause any computational difficulty in the simulation. On

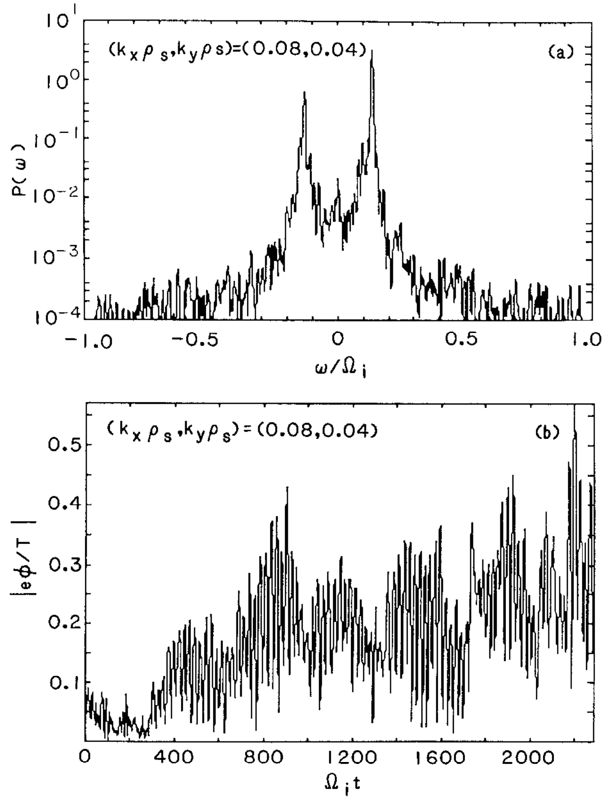

FIG. 3. Frequency spectrum (a) and amplitude evolution (b) of $e\Phi/T_e$ for $\rho_s/\Delta x_\perp = 0.1$ in a homogeneous plasma, when grid instability is present.

the other hand, it is also very comforting to know that the fluctuation energies for $|\omega| > |\omega_H|$ are orders of magnitude smaller.

The simulation results for the grid-induced instability in a homogeneous plasma with $\rho_s/\Delta x_\perp = 0.1$ are shown in Figs. 3a and 3b for $(k_x\rho_s, k_y\rho_s) \cong (0.08, 0.04)$. (Note that ω_H remains unchanged.) The normal mode frequencies and growth rate agree well with the predicted values of $\omega/\Omega_i = \pm 0.125 + i0.00021$ from Eq. (52). The fluctuation energy for this case is increased from the thermal level of $e\Phi/T_e = 24.6\ \%$, as given by Eq. (57), to well over $50\ \%$ because of the alisaing effects.

The issue of numerical instability caused by a large time step has also been examined. For $\omega_H(m=n)\,\Delta t = 3$ and $\rho_s/\Delta x_\perp = 0.25$, the numerical solution of

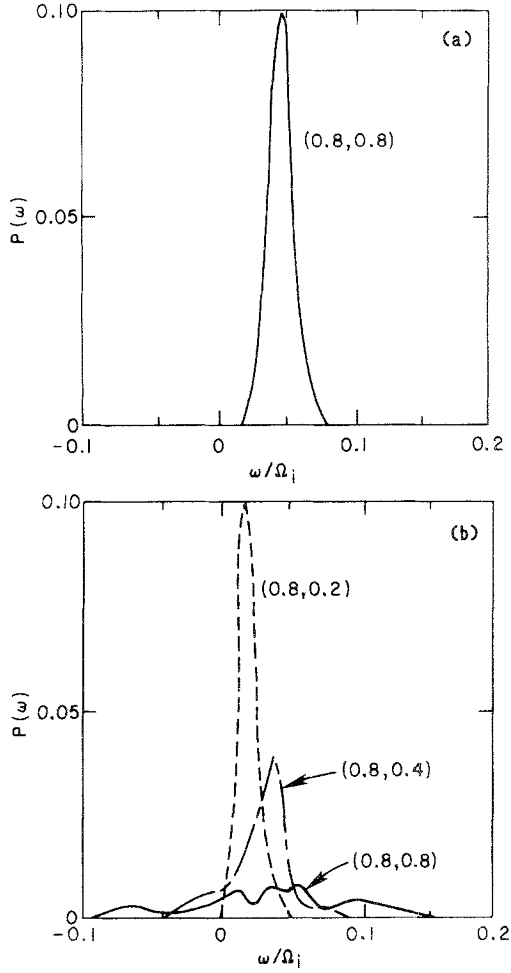

FIG. 4. Frequency spectra of $e\Phi/T_e$ for various values of $(k_x\rho_s, k_y\rho_s)$ in a $(32\times 32)\,\Delta x_\perp$ system (a) and a $(32\times 128)\,\Delta x_\perp$ system (b), when drift instability is present.

Eq. (52) indicates that $\mathrm{Im}\,\omega/\omega_H = 0.45$ for $(m, n) = (1, 1)$ and other highly unstable modes also exist in the system. In the simulation, a rapid increase of the electron kinetic energy has indeed been observed in just a few time steps.

The examples given here confirm the fact that the numerical properties of a gyrokinetic plasma are characterized by ω_H and ρ_s instead of ω_{pe} and λ_D as in the usual Vlasov description. As for the properties associated with a three-dimensional code, their verification is beyong the scope of the present paper and will be reported elsewhere.

Let us now discuss the case of an inhomogeneous plasma characterized by a constant density gradient. The simulation parameters are: $L_x \times L_y = (32 \times 32)\,\Delta x_\perp$, $N_{\mathrm{total}} = 128 \times 128$, $m_i/m_e = 1837$, $T_e/T_i = 4$, $a/\Delta x_\perp = 2$, $\theta_B = 0.002$, $\rho_s/\Delta x_\perp = 4.286$, $\kappa_n \rho_s = 0.214$, $(k_x\rho_s, k_y\rho_s) \cong (0.8m, 0.8n)$, and $\Omega_i \Delta t = 1.09$. These parameters give us the well-known drift instability in a shearless slab, which has been studied in detail in Refs. [20, 21]. Here, we would like to point out some of the salient features related to the simulation model. For example, the real frequency for the most unstable $(m = 1, n = 1)$ mode is $\mathrm{Re}\,\omega/\Omega_i = (k_y\rho_s)(\kappa_n\rho_s)[1 - (k_\perp\rho_i)^2]/[1 + (k_\perp\rho_s)^2] = 0.048$ [21]. It agrees well with the simulation results shown in Fig. 4a, for which we have used the $M = 4$ scheme (Fig. 1) in the code. When $M = 1$ is used instead, i.e., $\rho_i = 0$, the real frequency has been observed to shift upward to $\omega/\Omega_i = 0.075$. Thus, the numerical scheme given in Section III correctly represents the gyrophase-averaging procedure.

When the simulation volume is increased to $L_x \times L_y = (32 \times 128)\,\Delta x_\perp$, the resulting frequency spectra are characterized by an energy cascade from $k_\perp\rho_s \cong (0.8, 0.8)$ to longer wavelength modes, as shown in Fig. 4b. Interestingly, the frequencies for the enhanced modes seem to track their respective linear values with the characteristic of $\Delta\omega_{\mathbf{k}} \approx \omega_{\mathbf{k}}$. The "instantaneous" diffusion coefficient vs time, calculated from Eqs. (32) and (33), is given in Fig. 5. It describes the time evolution of particle diffusion from the linear stage ($\Omega_i \Delta t = 0$–200) of the instability to the steady-state part of the development. Since the background inhomogeneity is held constant in time, the latter represents the true value associated with the steady state, which, incidentally, is substantially smaller than the Bohm coefficient of $D = \frac{1}{16}$. To verify the results shown in Fig. 5, we have also compared their time averaged values with those from the test particle measurements. Excellent agreement has been obtained.

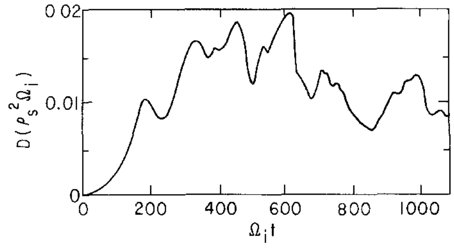

FIG. 5. Particle diffusion coefficient vs time in the presence of drift instability.

VII. Discussion and Conclusion

In this paper, we have presented an efficient computational scheme for studying low frequency microinstabilities in tokamaks. Critical numerical issues related to time step, grid spacing and noise level for the simulation plasma have also been examined in detail. We are convinced that gyrokinetic particle simulation scheme is indeed a viable approach and it will eventually help us in unravelling the mystery of anomalous transport in magnetically confined plasmas.

In fact, the two-dimensional $(x, y, \mu, v_{\|})$ gyrokinetic particle code described in Section VI has already been used to investigate various gradient-driven microinstabilities in slab geometry, providing us with some highly interesting results [20–22]. For example, it is found that nonlinear $\mathbf{E} \times \mathbf{B}$ trapping of the electrons is the dominant mechanism for the saturation of collisionless drift instabilities [20]. In the case of ion temperature gradient drift instabilities (η_i-modes), saturation comes from the nonlinearly generated zero-frequency current and pressure response, which cuts off the availability of the free energy source [22]. Most importantly, the simulation results have indicated that steady-state transport is intrinsically stochastic, in which electron-ion collisions also play a vital role [21]. As such, the parameter dependence is totally different from the estimates based on quasilinear diffusion. The latter in its various forms has been used for the development of scaling laws [35]. Comparison of our results with those based on the fluid equations will also help us in determining the regime of validity for such an approach in studying confinement problems.

Recently, gyrokinetic formalism has been generalized to toroidal geometry [36, 37]. It has also been shown that the aliases-induced numerical instabilities can be totally suppressed by magnetic perturbations [27] and that the thermal fluctuation level of shear-Alfven waves [38] can also be substantially reduced by the finite-β effects. These new developments will undoubtedly help us in achieving our ultimate goal, i.e., a 3D finite-β toroidal code to simulate tokamak discharges. Such a code can also find applications in other areas of plasma physics.

Let us conclude the paper by examining the kind of computer resources that one needs with the present model, using the Caltech tokamak [39] as an example. The revelant parameters are: $a = 16$ cm, $R = 45$ cm, $\rho_s = 0.15$–0.3 cm, $T_e = 25$–100 eV, and $\beta = 0.3$ %. From Eq. (60), we can choose $|e\Phi/T| \cong 1$ % as the maximum allowable level for the initial fluctuation. Since $k\rho_s \cong 0.1$ is roughly the smallest wave number here, Eq. (57) gives $N = 10^6$ as the required number of particles for the simulation. For an elongated 3D grid with $\Delta x_\perp \cong \rho_s$, it gives approximately 8 particles per cell. The memory and disk storage requirements for such a system is well within the capability of the Cray-II computer. Using a time step of $\Delta t = 1$ μs, which is sufficient to resolve the observed low frequency fluctuations, we can simulate 2 ms of the discharge with 2000 time steps of particle pushing. For a conservative figure of 50 μs per particle per time step on a Cray-II, the total CPU time is about 50 h. In our opinion, this is rather reasonable. For simulating large size tokamaks, e.g., TFTR at Princeton, an order of magnitude increase in the number of particles is needed, which may not be practical for the present generation of computers in terms of CPU time. On the other hand, one does not need to use the total cross section of the tokamak for simulating microinstabilities, which are believed to be active only in the outer region ($q > 1$) of the torus [19, 35, 39].

ACKNOWLEDGMENTS

The author gratefully acknowledges many very helpful discussions with Dr. W. M. Nevins. He is also indebted to Dr. L. Chen for suggesting the multiple spatial scale expansion scheme. Discussions with Dr. J. A. Krommes, Dr. C. Oberman, and Dr. W. M. Tang and their continuing interest in this work are also acknowledged. This work was supported by U.S. Department of Energy Contract DE-AC02-76CHO3073.

REFERENCES

1. W. W. LEE, *Phys. Fluids* **26**, 556 (1983).
2. D. H. E. DUBIN, J. A. KROMMES, C. R. OBERMAN, AND W. W. LEE, *Phys. Fluids* **26**, 3524 (1983).
3. A. B. LANGDON, *J. Comput. Phys.* **6**, 247 (1970).
4. A. B. LANGDON, *J. Comput. Phys.* **30**, 202 (1979).
5. W. W. LEE AND H. OKUDA, *J. Comput. Phys.* **26**, 139 (1978).
6. C. Z. CHENG AND H. OKUDA, *Phys. Rev. Lett.* **38**, 708 (1977).
7. W. W. LEE, Y. Y. KUO, AND H. OKUDA, *Phys. Fluids* **24**, 617 (1978).
8. W. W. LEE, W. M. NEVINS, H. OKUDA, AND R. B. WHITE, *Phys. Rev. Lett.* **43**, 347 (1979).
9. C. Z. CHENG AND H. OKUDA, *J. Comput. Phys.* **25**, 133 (1977).
10. H. OKUDA, W. W. LEE, AND C. Z. CHENG, *Comput. Phys. Commun.* **17**, 233 (1979).
11. A. FRIEDMAN, A. B. LANGDON, AND B. I. COHEN, *Comm. Plas. Phys. Contr. Fusion* **6**, 225 (1981); A. B. LANGDON, B. I. COHEN, AND A. FRIEDMAN, *J. Comput. Phys.* **51**, 107 (1983).
12. J. A. KROMMES, W. W. LEE, AND C. OBERMAN, *Phys. Fluids* **29**, 2421 (1986).
13. R. J. MASON, *J. Comput. Phys.* **41**, 233 (1981).
14. J. DENAVIT, *J. Comput. Phys.* **42**, 337 (1981).
15. D. C. BARNES, T. KAMIMURA, J.-N. LEBOEUF, AND T. TAJINA, *J. Comput. Phys.* **52**, 480 (1983).
16. B. I. COHEN, T. A. BRENGLE, D. B. CONLEY, AND R. P. FREIS, *J. Comput. Phys.* **38**, 45 (1980).
17. J. C. ADAM, A. GOURDIN-SERVENIERE, AND A. B. LANGDON, *J. Comput. Phys.* **47**, 229 (1982).
18. See, for example, I. STAKGOLD, *Boundary Value Problems of Mathematical Physics* (MacMillan, New York, 1967), Vol. 1.
19. See, for example, C. M. SURKO AND R. E. SLUSHER, *Science (Washington, D.C.)* **221**, 817 (1983).
20. W. W. LEE, J. A. KROMMES, C. R. OBERMAN, AND R. A. SMITH, *Phys. Fluids* **27**, 2652 (1984).
21. J. F. FEDERICI, W. W. LEE, AND W. M. TANG, *Phys. Fluids* **30**, 425 (1987).
22. W. W. LEE AND W. M. TANG, "Gyrokinetic Particle Simulation of Ion Temperature Gradient Drift Instability," Princeton University Plasma Physics Laboratory Report PPPL-2431 (May, 1987), submitted.
23. L. CHEN, W. W. LEE, F. W. PERKINS, AND Y. C. LEE, *Bull. Amer. Phys. Soc.* **25**, 966 (1980).
24. See, for example, J. M. DAWSON, *Rev. Mod. Phys.* **55**, 403 (1983).
25. See, for example, C. K. BIRDSALL AND A. B. LANGDON, *Plasma Physics via Computer Simulation* (McGraw–Hill, New York, 1985).
26. R. B. WHITE, *J. Comput. Phys.* **31**, 409 (1979).
27. W. W. LEE, "Feasibility of Gyrokinetic Particle Simulation of Tokamaks," Sherwood Theory Conference, New York, April 1986.
28. L. CHEN AND H. OKUDA, *J. Comput. Phys.* **19**, 339 (1975).

29. H. Abe, N. Sakairi, R. Itatani, and H. Okuda, *J. Compu. Phys.* **63**, 247 (1986).
30. H. Okuda and J. M. Dawson, *Phys. Fluids* **16**, 408 (1973)
31. J. B. Taylor and B. McNamara, *Phys. Fluids* **14**, 1492 (1971).
32 A B. Langdon, *Phys. Fluids* **22**, 163 (1979).
33. T. H. Dupree, *Phys Fluids* **11**, 2680 (1968).
34. See, for example, J. A. Krommes, in *Handbook of Plasma Physics* (North-Holland, Amsterdam, 1984), Vol. 2, p. 201.
35. See, for example, P. C. Liewer, *Nucl. Fusion* **25**, 543 (1985).
36. S.-C. Yang and D.-I. Choi, *Phys. Lett A* **108**, 25 (1985).
37. W. K. Hagen and E. A. Frieman, *Phys. Fluids* **28**, 2641 (1985).
38. W. W. Lee and R. D. Sydora, "Numerical Properties of a Finite-β Gyrokinetic plasma," Sherwood Theory Conference, San Diego, CA, April, 1987.
39. S. J. Zweden and R. W. Gould, *Nucl. Fusion* **23** (1983), 1625; **25**, 171 (1985).